Quantification and Determination of Normal ^{123}I-Meta Iodobenzylguanidine Heart-to-Mediastinum Ratio (HMR) from Cardiac SPECT/CT and Correlation with Planar HMR

Raza Alvi[1,2], Edward J. Miller[1–3], Taraneh Hashemi Zonouz[2], Veronica Sandoval[1], Noor Tariq[2], Rachel Lampert[2], Albert J. Sinusas[1–3], and Yi-Hwa Liu[1,2,4,5]

[1]Nuclear Cardiology, Yale-New Haven Hospital, New Haven, Connecticut; [2]Department of Internal Medicine (Cardiology), Yale University, New Haven, Connecticut; [3]Department of Radiology and Biomedical Imaging, Yale University, New Haven, Connecticut; [4]Department of Biomedical Imaging and Radiological Sciences, National Yang-Ming University, Taipei, Taiwan; and [5]Department of Biomedical Engineering, Chung Yuan Christian University, Taoyuan, Taiwan

Assessment of cardiac ^{123}I-meta iodobenzylguanidine (^{123}I-mIBG) uptake relies on the heart-to-mediastinum ratio (HMR) derived from planar images. We have developed novel semiautomated quantitative methodologies for assessing HMR from SPECT images using a dedicated cardiac multipinhole SPECT/CT system and determined the lower limit of normal (LLN) SPECT-derived HMR and the correlation to planar-derived HMR. **Methods:** Twenty-one healthy volunteers were injected with ^{123}I-mIBG and imaged using 2 different cameras. Planar images were acquired using a conventional SPECT camera equipped with parallel hole collimators, and hybrid SPECT/CT images were acquired using a dedicated cardiac SPECT system with 19 pinhole collimators interfaced with 64-slice CT. Planar HMR was calculated as per standard guidelines (manual traditional method) and elliptic region-of-interest (Elip-ROI) and region-growing (RG-ROI) techniques. SPECT HMR was quantified using a new method that incorporates various cardiac and mediastinal segmentation schemes in which upper and lower limits of the heart were determined from CT and the left ventricular ROI, and mean counts were calculated using Elip-ROI and RG-ROI techniques. Mean counts in mediastinal ROI were computed from a fixed volume in 3 different regions: upper mediastinum (UM), lower mediastinum (LM), and contralateral lung (CL). HMRs were processed by 2 observers, and reproducibility was assessed by intraclass correlation coefficient and Bland–Altman analysis. **Results:** Planar HMR calculated using the RG-ROI method showed highest intra- and interobserver levels of agreement compared with Elip-ROI and manual traditional methods. SPECT HMR calculated on the basis of UM, LM, and CL background regions showed excellent intra- and interobserver agreement. SPECT HMR with UM resulted in highest correlation (R = 0.91) with planar HMR compared with that with LM (R = 0.74) and CL (R = 0.73). The LLN of SPECT HMR with UM and that of planar HMR was calculated as 5.5 and 1.6, respectively. The normal values of SPECT-derived HMR and planar-derived HMR were correlated linearly. **Conclusion:** We reconfirmed the previous planar HMR threshold and determined SPECT LLN HMR for SPECT. Planar HMR can be estimated from SPECT HMR via a simple linear regression equation, allowing use of the new cardiac-dedicated SPECT camera for ^{123}I-mIBG imaging.

Key Words: ^{123}I labeled meta-iodobenzyl guanidine; SPECT; planar; heart-to-mediastinum ratio; mIBG quantification

J Nucl Med 2018; 59:652–658
DOI: 10.2967/jnumed.117.197152

Reduced myocardial sympathetic innervation is a prominent feature of heart failure (HF) due to posttranscriptional downregulation of the cardiac norepinephrine transporter (*1–3*). Myocardial imaging with ^{123}I-meta iodobenzylguanidine (^{123}I-mIBG), an analog of norepinephrine, is recognized as a useful tool for risk stratification of HF patients with reduced ejection fraction (*1–7*) and has been studied as a potential identifier of patients with increased risk for ventricular arrhythmic events (*4,6,8–13*). Previously published data have demonstrated that clinical utility of quantifying the heart-to-mediastinum ratio (HMR) and washout ratio (WR) from planar radionuclide images to assess myocardial ^{123}I-mIBG uptake provides a risk assessment of major adverse cardiac events and mortality (*1–13*). A low HMR value on delayed (3 h posttracer injection) images has been shown to be an independent predictor of ventricular tachyarrhythmia (*14,15*), appropriate implantable cardioverter defibrillator therapy (*16,17*), and sudden cardiac death (*18*) in HF patients. Moreover, an increased myocardial washout of ^{123}I-mIBG has been associated with poor prognosis (*7*). The ADMIRE-HF (AdreView Myocardial Imaging for Risk Evaluation in Heart Failure), a multicenter prospective trial of subjects with New York Heart Association II and III HF and left ventricular (LV) function of 35% or less, revealed an association of lower HMR of ^{123}I-mIBG uptake with higher 2-y incidence of cardiac events (*19*). In the ADMIRE-HF study, an HMR threshold of 1.6 derived from planar ^{123}I-mIBG images was used to dichotomize high- and low-risk patients based on the incidence of cardiac events. However, normal limits of HMRs derived from ^{123}I-mIBG SPECT images have not been extensively investigated.

Despite the proven prognostic value of ^{123}I-mIBG in patients with HF, there remain limitations to the use of ^{123}I-mIBG imaging (*4*). One of the common limitations is the variation among different methods used for HMR and WR quantifications. This variation can be caused by image acquisition time and duration, location, and size of the heart and mediastinal region of interest (ROI) (*13,20,21*) as

Received Jun. 7, 2017; revision accepted Aug. 30, 2017.
For correspondence or reprints contact: Yi-Hwa Liu, Section of Cardiovascular Medicine, Department of Internal Medicine, Yale University School of Medicine, New Haven, CT 06520.
E-mail: yi-hwa.liu@yale.edu
Published online Sep. 15, 2017.

well as the level of expertise and experience for WR calculation (*22*). Additionally, SPECT ^{123}I-mIBG quantification is technically challenging because of the regional variation of myocardial ^{123}I-mIBG uptake, potential artifacts related to radioactivity in adjacent lung and liver areas, and reduced global ^{123}I-mIBG uptake that is commonly observed in patients with severe systolic dysfunction (*23*). Although cardiac-dedicated SPECT cameras with solid-state detectors and multipinhole collimators provide superior 3-dimensional (3D) image resolution in the small cardiac ROI, these imaging devices are not capable of acquiring traditional 2-dimensional planar images due to the nonconventional geometry and magnification of multipinhole collimation, limiting the use of these new imaging devices for ^{123}I-mIBG imaging.

The purpose of this study was to develop novel semiautomated quantitative methodology for ^{123}I-mIBG HMR quantification using a dedicated cardiac SPECT/CT camera equipped with solid-state detectors and pinhole collimators and compare SPECT-derived HMR to traditional planar-derived HMR in a cohort of normal patients. In addition, we sought to assess the reliability of planar and SPECT ^{123}I-mIBG quantifications using traditional as well as automated software and determine the lower limits of normal (LLNs) SPECT-derived ^{123}I-mIBG HMRs from normal subjects.

MATERIALS AND METHODS

After the approval of the Institutional Review Board, we enrolled 21 healthy normal volunteers (10 men and 11 women) between the ages of 32 and 64 y (48 ± 12 y) with mean body mass index of 26.3 ± 4.9 kg/m^2. All subjects signed a written informed consent form. Subjects who were pregnant or with cognitive impairment, any heart disease, or other significant illness or medications that could influence the sympathetic activity of the heart were excluded from this study. All subjects had a normal baseline 12-lead electrocardiogram and were injected with ^{123}I-mIBG (209 ± 44 MBq; AdreView [GE Healthcare]) after administration of Lugol's solution (100 mg). Planar and SPECT/CT images were acquired for all subjects (Fig. 1).

Planar MIBG Image Acquisition and Analysis

Planar images with a 128 × 128 matrix and 3.3 × 3.3 mm^2 pixel size were acquired at 30 min (early images) and 180 min (late or delayed images) after ^{123}I-mIBG injection, with the patient supine, for 10 min using a dual-head SPECT system equipped with low-energy high-resolution collimators (Infinia; GE Healthcare). HMR was assessed with 3 different methods. For the first method, as per the Adreview package insert (traditional method), HMR was calculated from planar ^{123}I-mIBG images on which heart and mediastinal ROIs were manually drawn using XELERIS postprocessing software (Infinia; GE Healthcare). The heart ROI was determined by the epicardial border visualized using the medial aspect of lower part of the lungs for an anatomic guidance. The lung apices were visually estimated using a horizontal line intersected by the vertical line equidistant from the medial aspects of upper part of the lungs. A square ROI of 7 × 7 pixels was centered and drawn at the location with the lowest count visualized along the vertical line below the horizontal line intersection (Fig. 2). For the second method (elliptic ROI method), HMR was calculated using the Yale Cardiac Quantification (Yale-CQ) software in which an initial elliptic ROI was placed over the heart and the elliptic ROI was adjusted in length, width, and axial angle to visually fit the heart region using a user graphical interface, and a square ROI of 7 × 7 pixels was centered and drawn at the location with the lowest counts along 12 pixels of the vertical line starting at 4 pixels below the horizontal line intersection. For the third method (region growing), the heart ROI was further refined and recalculated using a region-growing algorithm developed at Yale. For the mediastinal ROI, a horizontal line was placed on the lung apices, and a box of 7 × 7 pixels was automatically determined by the Yale-CQ software. Using the above 3 methods for determination of the heart and mediastinal ROIs, HMR was calculated by dividing the mean count (counts/pixel) in the heart ROI by that in the mediastinal ROI (Figs. 1 and 2A–2D).

^{123}I-mIBG WR was calculated from early and late (delayed) planar images without background correction, WR (%) = $(H_e\text{-}H_l)/H_e \times 100$, and with background correction, $WR_{BKG\text{-}corrected}$ (%) = $[(H_e\text{-}M_e) - (H_l\text{-}M_l)]/(H_e\text{-}M_e) \times 100$, where H represents the mean count from the heart ROI and M denotes the mean count in the mediastinal ROI for early (e) and late (l) ^{123}I-mIBG planar images (*24*).

SPECT ^{123}I-mIBG Image Acquisition and Analysis

SPECT raw images with a 32 × 32 matrix and 2.5 × 2.5 mm^2 pixel size were acquired for 15 min at 30, 90, 120, and 180 min after ^{123}I-mIBG tracer injection using a stationary cardiac-dedicated hybrid SPECT/CT scanner equipped with cadmium zinc telluride (CZT) detectors and 19 tungsten pinhole collimators (Discovery NM/CT 570c; GE Healthcare). A noncontrast CT scan used for SPECT attenuation correction was acquired with 120 kVp, 50 mA, a pitch of 0.984, a slice thickness of 2.5 mm, and a rotation speed of 0.4 s and was reconstructed using filtered backprojection with a voxel size of 0.977 mm^3. SPECT images were reconstructed with a matrix size of 70 × 70 and pixel size of 3.2 × 3.2 mm^2 using the maximum-likelihood expectation maximization algorithm incorporated with the CT-based attenuation correction. For SPECT-derived HMR quantification, the upper and lower limits of the heart were determined by the central tranaxial slice of CT images coregistered with SPECT, and the ROI of the LV myocardium was automatically segmented using a previously published bimodal median threshold algorithm (*25,26*). Mean counts in the LV myocardium were calculated from the LV regions segmented, and background mean counts were calculated from 3 different regions (upper mediastinum [UM], lower mediastinum [LM], and contralateral lung [CL]) each with a fixed volume of 5 × 5 × 5 voxels manually defined (Figs. 1 and 2E–2H).

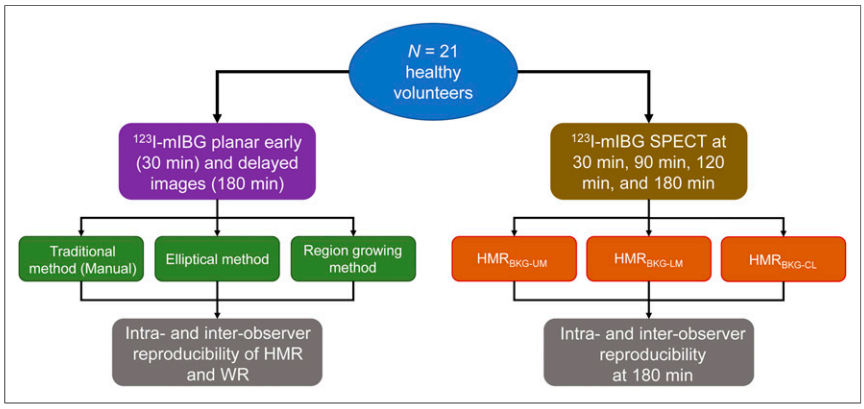

FIGURE 1. Flowchart of patient study, ^{123}I-mIBG planar and SPECT imaging, and data analyses.

Reproducibility of HMR Quantification

Analyses of intra- and interobserver agreements were performed to evaluate the reproducibility of HMR and WR quantifications. Intraobserver variability was assessed by a

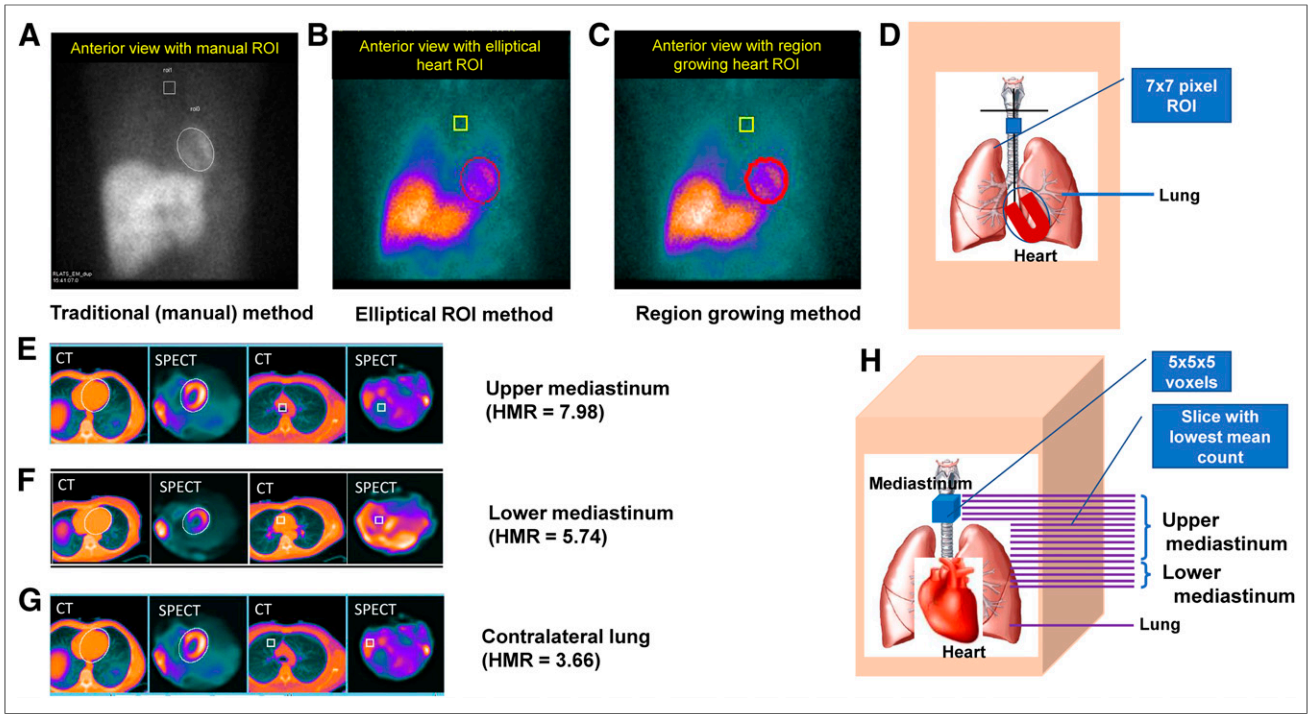

FIGURE 2. Planar-HMR quantification methods: planar images with heart and mediastinal ROIs (A–C) and schematics showing relative positions of heart and mediastinal regions in 2D (D). SPECT HMR quantification methods from fused SPECT/CT images: coregistered central SPECT and CT slices of heart and mediastinal regions (E–G) and schematics showing relative positions of heart and 2 different mediastinal regions in 3D (H).

single operator (A), who processed all images twice with 4 wk apart to avoid recall bias. For interobserver variability, the images were processed independently by 2 different operators (A and B). The LLN was calculated by mean – 2 × SD.

Statistical Analysis

All statistical analyses were performed using Microsoft Excel and SPSS (Statistical Package for the Social Sciences) software. Continuous variables were expressed as mean ± SD. Paired t test and 1-way ANOVA were used for comparisons among variables. Quantification performed by different operators were compared using the linear regression equation and correlation analysis. Intraclass correlation coefficient (ICC) was calculated to assess the reliability measure with the ICC being classified as poor, fair, good, and excellent based on values of less than 0.49, 0.49 to 0.59, 0.60 to 0.74, and greater than 0.74, respectively (*27*). Bland–Altman plots were used to assess agreements between the quantified data (*28*).

RESULTS

Planar HMR quantified using the region-growing method resulted in highest intraobserver (Table 1; Supplemental Figs. 1 and 2 [supplemental

TABLE 1
Early and Delayed Planar HMR for Intra- and Interobserver Analysis

	Traditional method		Elliptic method		Region-growing method	
Reproducibility	Early HMR	Delayed HMR	Early HMR	Delayed HMR	Early HMR	Delayed HMR
Intraobserver						
First measurement	2.01 ± 0.18	2.12 ± 0.25	1.97 ± 0.17	2.09 ± 0.22	1.99 ± 0.19	2.14 ± 0.25
Second measurement	1.98 ± 0.19	2.08 ± 0.26	1.95 ± 0.16	2.07 ± 0.21	1.97 ± 0.17	2.12 ± 0.23
ICC	0.89	0.87	0.94	0.93	0.97	0.97
95% confidence interval	0.67–0.96	0.66–0.97	0.72–0.99	0.74–0.98	0.92–0.99	0.82–0.99
Interobserver						
First observer	2.01 ± 0.20	2.12 ± 0.25	1.97 ± 0.17	2.13 ± 0.23	1.99 ± 0.19	2.14 ± 0.25
Second observer	1.97 ± 0.23	2.09 ± 0.26	1.98 ± 0.19	2.12 ± 0.25	2.00 ± 0.20	2.11 ± 0.25
ICC	0.80	0.86	0.95	0.95	0.98	0.98
95% confidence interval	0.52–0.92	0.62–0.95	0.92–0.99	0.91–0.99	0.95–0.99	0.94–0.99

TABLE 2
Washout Rates for Intra- and Interobserver Analysis

Reproducibility	Traditional method		Elliptic method		Region-growing method	
	WR	$WR_{BKG\text{-}corrected}$	WR	$WR_{BKG\text{-}corrected}$	WR	$WR_{BKG\text{-}corrected}$
Intraobserver						
First measurement	20.7 ± 5.1	15.0 ± 9.9	21.6 ± 4.5	17.0 ± 8.9	21.8 ± 4.6	17.6 ± 9.1
Second measurement	21.5 ± 4.9	16.5 ± 9.5	22.6 ± 5.1	19.9 ± 8.3	22.8 ± 5.3	20.2 ± 8.7
ICC	0.84	0.80	0.92	0.82	0.94	0.86
95% confidence interval	−0.16–0.96	−0.18–0.94	0.76–0.96	0.55–0.93	0.79–0.97	0.64–0.94
Interobserver						
First observer	20.7 ± 5.1	15.0 ± 9.9	21.6 ± 4.5	17.0 ± 8.9	21.8 ± 4.6	17.6 ± 9.1
Second observer	21.5 ± 4.6	18.1 ± 8.1	21.3 ± 5.0	17.4 ± 9.0	21.6 ± 5.0	18.0 ± 9.1
ICC	0.86	0.75	0.94	0.80	0.96	0.85
95% confidence interval	0.60–0.97	0.50–0.92	0.84–0.97	0.51–0.92	0.88–0.98	0.60–0.94

materials are available at http://jnm.snmjournals.org]) and interobserver (Table 1; Supplemental Figs. 3 and 4) reproducibilities as compared with elliptic ROI and traditional manual methods. There was no significant difference among mean WRs calculated using the 3 methods. However, WRs obtained from the region-growing method were more reproducible and precise (more repeatable) than those obtained from the elliptic ROI method and traditional methods in terms of intra- (ICC = 0.94) and interobserver (ICC = 0.96) variabilities (Table 2). For all 3 methods, WRs without background correction were more reproducible and precise than those with background correction (Table 2; Supplemental Figs. 5 and 6). The LLN of HMR derived from planar images using the 3 methods above ranged from 1.56 to 1.64.

SPECT HMRs calculated on the basis of the upper mediastinum ($HMR_{BKG\text{-}UM}$), lower mediastinum ($HMR_{BKG\text{-}LM}$), and contralateral lung ($HMR_{BKG\text{-}CL}$) background regions showed excellent intra- and interagreements (Table 3; Supplemental Fig. 7). However, HMR calculated using the UM background resulted in highest linear correlation with region-growing ROI planar HMR (R = 0.91) compared with those calculated using the LM (R = 0.74) and CL background (R = 0.73) as shown in Figure 3. The LLN of the HMR derived from $HMR_{BKG\text{-}UM}$ was higher than those derived from $HMR_{BKG\text{-}LM}$ and $HMR_{BKG\text{-}CL}$ (Table 3). Table 4 shows the mean $HMR_{BKG\text{-}UM}$ and LLN processed by observer A1 at 4 different tracer injection times (t = 30, 90, 120, and 180 min). As seen, SPECT-derived HMR and LLN increased as a function of the SPECT imaging time. Paired HMR comparisons between 120, 90, and 30 min versus 180 min are shown in Figure 4. The correlation between HMR at 120 min and HMR at 180 min was highest among these 3 paired comparisons. The difference between HMRs at 120 and 180 min was not significantly different, and LLNs at 120 and 180 min were similar (5.1 and 5.6, respectively). The normal values of SPECT-derived HMR and planar-derived HMR were linearly correlated by $y = 3.77 \times -0.21$, where y = SPECT-derived HMR and x = planar-derived HMR.

DISCUSSION

We have reported herein the quantification reproducibility and precision of ^{123}I-mIBG myocardial uptake from planar and SPECT images using traditional methods and the semiautomated Yale

TABLE 3
SPECT HMR and Intra- and Interobserver Analysis

Reproducibility	$HMR_{BKG\text{-}UM}$	$HMR_{BKG\text{-}LM}$	$HMR_{BKG\text{-}CL}$
Intraobserver			
First measurement	8.0 ± 1.2	5.7 ± 1.3	3.9 ± 1.3
Second measurement	7.9 ± 1.2	5.6 ± 1.3	4.0 ± 1.3
Mean LLN	(5.6 + 5.6)/2 = 5.6	(3.0 + 3.0)/2 = 3.0	(1.4 + 1.4)/2 = 1.4
ICC	0.96	0.96	0.95
95% confidence interval	0.909–0.985	0.911–0.995	0.893–0.985
Interobserver			
First observer	8.0 ± 1.2	5.7 ± 1.3	3.9 ± 1.3
Second observer	8.0 ± 1.3	5.5 ± 1.3	4.0 ± 1.25
Mean LLN	(5.6 + 5.4)/2 = 5.5	(3.0 + 3.0)/2 = 3.0	(1.4 + 1.5)/2 = 1.45
ICC	0.95	0.97	0.95
95% confidence interval	0.903–0.989	0.941–0.994	0.894–0.983

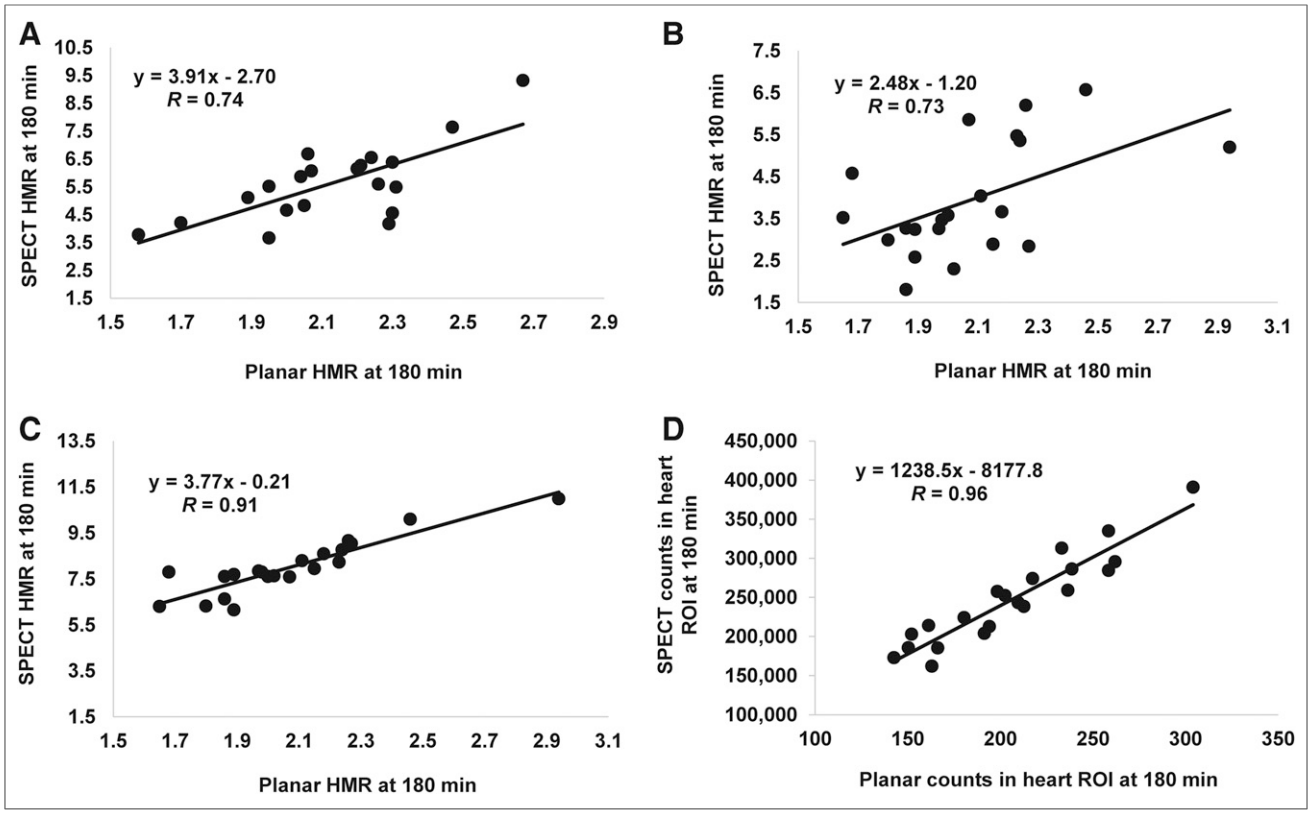

FIGURE 3. Correlations between planar HMR quantified using region-growing ROI and SPECT HMRs calculated on basis of 3 background (BKG) regions: $HMR_{BKG\text{-}LM}$ (A), $HMR_{BKG\text{-}CL}$ (B), and $HMR_{BKG\text{-}UM}$ (C), and correlation between planar and SPECT mean counts in heart ROI (D).

approach. In the normal low-risk population, we have determined the normal limits of myocardial ^{123}I-mIBG uptake from planar and SPECT images and established a linear correlation between the planar and SPECT HMRs determined using various ^{123}I-mIBG quantification methods. The present study also demonstrated that the intra- and interobserver reproducibilities for the ^{123}I-mIBG image quantifications were excellent.

Although we have presented various unique approaches to the quantification of ^{123}I-mIBG myocardial uptake, substantial efforts had been made by others to standardize the methods for HMR quantification from ^{123}I-mIBG myocardial scintigraphy. For planar mIBG imaging, most previous investigators used traditional manual methods similar to those we used for HMR quantification (*8,22,23,29*). Although planar images are comparatively easier to acquire and quantify, SPECT imaging for ^{123}I-mIBG has considerable benefits because of its potential to evaluate regional heterogeneities of the myocardial mIBG uptake above and beyond the HMR and WR assessments. Moreover, with SPECT imaging superimposition of the anatomic structures seen in 2-dimensional planar images (e.g., lungs overlapping the heart) can be minimized and identification of the heart limits in 3D is feasible, leading to more accurate quantification (a measurement close to the true value). For SPECT ^{123}I-mIBG quantification, several different methods have been reported. Van der Veen et al. assessed cardiac innervation using volumetric quantification of ^{123}I-mIBG with planar and SPECT acquisitions in 54 patients referred for imaging before placement of an implantable cardioverter defibrillator. In that study, ^{123}I-mIBG SPECT HMR was derived from an automated system using midventricular-short-axis and vertical- and horizontal-long-axis SPECT slices to create 3D volume of interest for the heart and mediastinum regions (*29*). Another study by Bellevre et al. reported ^{123}I-MIBG HMR quantification using a CZT-based camera (D-SPECT; SPECTRUM Dynamic Medical) with a dual-isotope protocol (^{123}I and ^{99m}Tc) and compared the HMR with that quantified from the conventional planar images, which were acquired using an Anger-SPECT camera with low-energy and high-resolution collimators. The planar HMR was quantified using the traditional method by drawing the ROI manually on the LV and over the UM area, and SPECT ^{123}I-MIBG HMR was quantified using the same ROI drawn on the ^{99m}Tc SPECT images (*30*). In our study, however, we used the traditional method as well as the semiquantitative methods for planar HMR calculation and compared the results with the SPECT HMRs obtained by incorporating the SPECT and CT image coregistration. In addition, there were 3 other reports that assessed the cardiac sympathetic denervation based on the mismatch score of ^{123}I-mIBG and ^{99m}Tc-labeled perfusion images using a severity measure on the standard 17-segment model (*8,23,31*). In our study, the planar images were acquired using a dual-head SPECT system with low-energy high-resolution

TABLE 4
LLN for SPECT $HMR_{BKG\text{-}UM}$

Time after injection	t = 180 min	t = 120 min	t = 90 min	t = 30 min
Mean ± SD	8.0 ± 1.2	7.3 ± 1.1	6.8 ± 1.1	5.5 ± 1.1
LLN	5.6	5.1	4.6	3.3

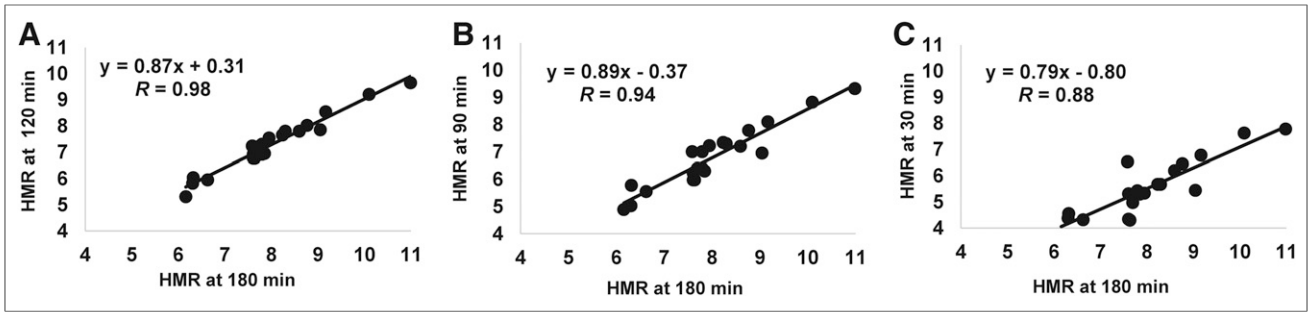

FIGURE 4. Correlations of SPECT HMR_{BKG-UM} at 180 min versus (A) 120 min, (B) 90 min, and (C) 30 min, after ^{123}I-mIBG injection.

collimators. Although the HMR values can be varied by different types of collimators and imaging systems used, Nakajima et al. have demonstrated that standardization of HMR using a cardiac calibration phantom method is feasible (*32*).

In the present study, we used semiautomated software involving the placement of an automatically adjustable elliptic-shaped ROI around the heart using the region-growing method. An alternative semiautomated elliptic ROI method was also introduced in this report for HMR quantification, although this approach was found to be inferior to the region-growing method in terms of reproducibility and precision, presumably due to the variability in the ROI placement using the elliptic method. More specifically, unlike the averaged mediastinum ROI counts, the elliptic-shaped ROI being placed around the heart can be variable in width and shape, as well as angular placement, and therefore somewhat operator dependent (*27*). However, this variability can be reduced by the region-growing method, which automatically adjusts the elliptic ROI around the heart using a heuristic region-growing algorithm, thereby minimizing intra- and interobserver variabilities. In comparison, the traditional manual method is highly operator-dependent and is less reliable and reproducible than both automated methods (elliptic ROI and region-growing ROI). These findings were further confirmed by the ICCs and Bland–Altman analyses in this report. More specifically, the ICC, a measure of reliability, was highest using the region-growing ROI method as compared with the elliptic ROI and traditional methods.

For SPECT HMR quantification, all the 3 ROI methods showed excellent intra- and interobserver reproducibility, and reliability as indicated by ICC greater than 0.90 for all 3 methods, and by the narrow limits of agreement defined by Bland–Altman analysis. These results were somewhat expected, however, because all these 3 methods were implemented in an automated manner, in which HMR was calculated with a minimal user interaction with the software. In this study, the SPECT region-growing ROI method using the UM location for calculations of the background and SPECT HMR resulted in the strongest linear correlation with planar HMR. Lower correlations between planar HMR and SPECT HMR were observed when the LM or CL was used as background in the HMR calculation (Figs. 3A–3C). This difference was attributed to the variation of the mean counts calculated from these 3 background ROIs. The best correlation between the planar-derived and SPECT-derived HMRs was noticed when the UM ROI was used for background (Fig. 3C). Also, as seen in Figure 3D, there was a strong linear correlation between the SPECT and planar mean counts from the heart ROI, which was not affected by the background. The variation of the mean counts calculated from the background ROIs mentioned above usually exists but may be more modest for CZT SPECT cameras with limited field of view. This background variation may in turn lead to the reduction of ICC for WR (Table 2). In the present study, we selected the most upper SPECT slices near the UM region that could be reliably reconstructed by the CZT SPECT so that a good correlation between the planar and SPECT HMR was feasible. However, the UM region we used for SPECT HMR calculation may not be the same region commonly used for planar HMR calculation.

The LLN HMR (1.56–1.64) derived from the planar images in this study was consistent with the previous HMR cutoff of 1.6 proposed by Jacobson et al. (*4*) for optimal risk stratification of HF patients. For SPECT images, the HMR LLN calculated with the UM ROI was higher than those with the LM or CL ROIs (Table 3). This HMR difference can be attributable to the increased mean counts from the background structures in the LM or CL ROIs. As demonstrated in this study, the SPECT-derived HMR that incorporated the UM background ROI and region-growing ROI method provided the highest correlation with the planar-derived HMR along with best reproducibility and reliability. Thus, it may be feasible to estimate the normal values of SPECT-derived HMR from planar-derived HMR or vice versa via the linear regression equation (SPECT_HMR = 3.77 × planar_HMR − 0.21) established in the present study.

The application of myocardial ^{123}I-mIBG SPECT imaging in the risk stratification of patients with ischemic heart disease has been focused on the detection of sympathetic innervation based on the calculation of HMR or WR. Although a strong association between regional innervation abnormality and susceptibility to arrhythmias has been demonstrated particularly in the ischemic setting (*10,12,19,33,34*), further studies are needed to evaluate the utility of SPECT-based HMR value in predicting future cardiac arrhythmic events. In the current study, we have introduced a new semiautomated method for reproducible quantification of ^{123}I-mIBG HMR and WR from planar and SPECT images. Our results showed a linear relationship between planar and SPECT HMR values, indicating the feasibility of estimating the normal values of SPECT-derived parameters from planar images or vice versa. However, this study cohort comprised evaluation of all normal healthy volunteers; hence, further validation in abnormal individuals is warranted in future investigation.

CONCLUSION

The quantification of ^{123}I-mIBG HMR and WR from SPECT images using the semiautomated methods was extremely reproducible and precise. The LLN HMRs quantified from SPECT and planar images were derived using normal volunteers. The LLN of planar HMR was consistent with the HMR cutoff used for the risk

stratification in the ADMIRE-HF study. The LLN HMR quantified from SPECT images is greater than that from planar images. It may be feasible to translate ^{123}I mIBG HMR values from SPECT into a value for conventional planar HMR value via a simple linear equation.

DISCLOSURE

This work was supported in part by an Investigator Initiated Trial Grant from GE Healthcare, Inc., and a Grant-in-Aid research grant from the American Heart Association (14GRNT19040010). No other potential conflict of interest relevant to this article was reported.

ACKNOWLEDGMENTS

We thank Vera Tsatkin, Ramesh Fazzone-Chettiar, and Stephanie Thorn, PhD, for their technical assistance in this study. This research was presented in part at the Annual Meeting of American College of Cardiology April 2–4, 2016 (ACC 2016), Chicago, Illinois.

REFERENCES

1. Agostini D, Verberne HJ, Burchert W, et al. I-123-mIBG myocardial imaging for assessment of risk for a major cardiac event in heart failure patients: insights from a retrospective European multicenter study. *Eur J Nucl Med Mol Imaging.* 2008;35:535–546.
2. Merlet P, Valette H, Dubois-Rande JL, et al. Prognostic value of cardiac metaiodobenzylguanidine imaging in patients with heart failure. *J Nucl Med.* 1992;33: 471–477.
3. Nakata T, Miyamoto K, Doi A, et al. Cardiac death prediction and impaired cardiac sympathetic innervation assessed by MIBG in patients with failing and nonfailing hearts. *J Nucl Cardiol.* 1998;5:579–590.
4. Jacobson AF, Senior R, Cerqueira MD, et al. Myocardial iodine-123 metaiodobenzylguanidine imaging and cardiac events in heart failure. Results of the prospective ADMIRE-HF (AdreView Myocardial Imaging for Risk Evaluation in Heart Failure) study. *J Am Coll Cardiol.* 2010;55:2212–2221.
5. Nakata T, Nakajima K, Yamashina S, et al. A pooled analysis of multicenter cohort studies of ^{123}I-mIBG imaging of sympathetic innervation for assessment of long-term prognosis in heart failure. *JACC Cardiovasc Imaging.* 2013;6:772–784.
6. Narula J, Gerson M, Thomas GS, Cerqueira MD, Jacobson AF. ^{123}I-MIBG imaging for prediction of mortality and potentially fatal events in heart failure: The ADMIRE-HFX Study. *J Nucl Med.* 2015;56:1011–1018.
7. Verberne HJ, Brewster LM, Somsen GA, van Eck-Smit BL. Prognostic value of myocardial ^{123}I-metaiodobenzylguanidine (MIBG) parameters in patients with heart failure: a systematic review. *Eur Heart J.* 2008;29:1147–1159.
8. Arora R, Ferrick KJ, Nakata T, et al. I-123 MIBG imaging and heart rate variability analysis to predict the need for an implantable cardioverter defibrillator. *J Nucl Cardiol.* 2003;10:121–131.
9. Inoue H, Zipes DP. Results of sympathetic denervation in the canine heart: supersensitivity that may be arrhythmogenic. *Circulation.* 1987;75:877–887.
10. Minardo JD, Tuli MM, Mock BH, et al. Scintigraphic and electrophysiological evidence of canine myocardial sympathetic denervation and reinnervation produced by myocardial infarction or phenol application. *Circulation.* 1988;78:1008–1019.
11. Nagahara D, Nakata T, Hashimoto A, et al. Predicting the need for an implantable cardioverter defibrillator using cardiac metaiodobenzylguanidine activity together with plasma natriuretic peptide concentration or left ventricular function. *J Nucl Med.* 2008;49:225–233.
12. Simões MV, Barthel P, Matsunari I, et al. Presence of sympathetically denervated but viable myocardium and its electrophysiologic correlates after early revascularised, acute myocardial infarction. *Eur Heart J.* 2004;25:551–557.
13. Tamaki S, Yamada T, Okuyama Y, et al. Cardiac iodine-123 metaiodobenzylguanidine imaging predicts sudden cardiac death independently of left ventricular ejection fraction in patients with chronic heart failure and left ventricular systolic dysfunction: results from a comparative study with signal-averaged electrocardiogram, heart rate variability, and QT dispersion. *J Am Coll Cardiol.* 2009;53:426–435.
14. Agostini D, Carrio I, Verberne HJ. How to use myocardial ^{123}I-MIBG scintigraphy in chronic heart failure. *Eur J Nucl Med Mol Imaging.* 2009;36:555–559.
15. Paul M, Schafers M, Kies P, et al. Impact of sympathetic innervation on recurrent life-threatening arrhythmias in the follow-up of patients with idiopathic ventricular fibrillation. *Eur J Nucl Med Mol Imaging.* 2006;33:866–870.
16. Al Badarin FJ, Wimmer AP, Kennedy KF, Jacobson AF, Bateman TM. The utility of ADMIRE-HF risk score in predicting serious arrhythmic events in heart failure patients: incremental prognostic benefit of cardiac ^{123}I-mIBG scintigraphy. *J Nucl Cardiol.* 2014;21:756–762.
17. Bax JJ, Kraft O, Buxton AE, et al. 123 I-mIBG scintigraphy to predict inducibility of ventricular arrhythmias on cardiac electrophysiology testing: a prospective multicenter pilot study. *Circ Cardiovasc Imaging.* 2008;1:131–140.
18. Boogers MJ, Borleffs CJ, Henneman MM, et al. Cardiac sympathetic denervation assessed with 123-iodine metaiodobenzylguanidine imaging predicts ventricular arrhythmias in implantable cardioverter-defibrillator patients. *J Am Coll Cardiol.* 2010;55:2769–2777.
19. Sasano T, Abraham MR, Chang KC, et al. Abnormal sympathetic innervation of viable myocardium and the substrate of ventricular tachycardia after myocardial infarction. *J Am Coll Cardiol.* 2008;51:2266–2275.
20. Verberne HJ, Feenstra C, de Jong WM, Somsen GA, van Eck-Smit BL, Busemann Sokole E. Influence of collimator choice and simulated clinical conditions on ^{123}I-MIBG heart/mediastinum ratios: a phantom study. *Eur J Nucl Med Mol Imaging.* 2005;32:1100–1107.
21. Verberne HJ, Habraken JB, van Eck-Smit BL, Agostini D, Jacobson AF. Variations in ^{123}I-metaiodobenzylguanidine (MIBG) late heart mediastinal ratios in chronic heart failure: a need for standardisation and validation. *Eur J Nucl Med Mol Imaging.* 2008;35:547–553.
22. Okuda K, Nakajima K, Hosoya T, et al. Semi-automated algorithm for calculating heart-to-mediastinum ratio in cardiac Iodine-123 MIBG imaging. *J Nucl Cardiol.* 2011;18:82–89.
23. Travin MI, Henzlova MJ, van Eck-Smit BL, et al. Assessment of ^{123}I-mIBG and ^{99m}Tc-tetrofosmin single-photon emission computed tomographic images for the prediction of arrhythmic events in patients with ischemic heart failure: intermediate severity innervation defects are associated with higher arrhythmic risk. *J Nucl Cardiol.* 2017;24:377–391.
24. Flotats A, Carrio I, Agostini D, et al. Proposal for standardization of ^{123}I-metaiodobenzylguanidine (MIBG) cardiac sympathetic imaging by the EANM Cardiovascular Committee and the European Council of Nuclear Cardiology. *Eur J Nucl Med Mol Imaging.* 2010;37:1802–1812.
25. Liu Y-H, Hashemi-Zonouz T, Sandoval V, Lampert R, Sinusas AJ. Normal limits of heart-to-mediastinum ratio (HMR) of I-123 MIBG uptake quantified from high sensitivity (HS) and high-resolution (HR) SPECT/CT. *J Am Coll Cardiol.* 2016;67:1822.
26. Liu Y-H, Wu J, Liu C, Sinusas AJ. Planar versus SPECT quantification of the heart-to-mediastinum ratio from I-123-MIBG sympathetic cardiac SPECT imaging: accuracy as assessed by computer simulations. *Eur Heart J Cardiovasc Imaging.* 2015;16:i25.
27. Veltman CE, Boogers MJ, Meinardi JE, et al. Reproducibility of planar ^{123}I-meta-iodobenzylguanidine (MIBG) myocardial scintigraphy in patients with heart failure. *Eur J Nucl Med Mol Imaging.* 2012;39:1599–1608.
28. Bland JM, Altman DG. Statistical methods for assessing agreement between two methods of clinical measurement. *Lancet.* 1986;1:307–310.
29. van der Veen BJ, Al Younis I, de Roos A, Stokkel MP. Assessment of global cardiac I-123 MIBG uptake and washout using volumetric quantification of SPECT acquisitions. *J Nucl Cardiol.* 2012;19:752–762.
30. Bellevre D, Manrique A, Legallois D, et al. First determination of the heart-to-mediastinum ratio using cardiac dual isotope (^{123}I-MIBG/^{99m}Tc-tetrofosmin) CZT imaging in patients with heart failure: the ADRECARD study. *Eur J Nucl Med Mol Imaging.* 2015;42:1912–1919.
31. Clements IP, Garcia EV, Chen J, Folks RD, Butler J, Jacobson AF. Quantitative iodine-123-metaiodobenzylguanidine (MIBG) SPECT imaging in heart failure with left ventricular systolic dysfunction: Development and validation of automated procedures in conjunction with technetium-99m tetrofosmin myocardial perfusion SPECT. *J Nucl Cardiol.* 2016;23:425–435.
32. Nakajima K, Okuda K, Matsuo S, et al. Standardization of metaiodobenzylguanidine heart to mediastinum ratio using a calibration phantom: effects of correction on normal databases and a multicentre study. *Eur J Nucl Med Mol Imaging.* 2012;39:113–119.
33. McGhie AI, Corbett JR, Akers MS, et al. Regional cardiac adrenergic function using I-123 meta-iodobenzylguanidine tomographic imaging after acute myocardial infarction. *Am J Cardiol.* 1991;67:236–242.
34. Stanton MS, Tuli MM, Radtke NL, et al. Regional sympathetic denervation after myocardial infarction in humans detected noninvasively using I-123-metaiodobenzylguanidine. *J Am Coll Cardiol.* 1989;14:1519–1526.